

Constraining the initial temperature and shear viscosity in a hybrid hydrodynamic model of $\sqrt{s_{NN}}=200$ GeV Au+Au collisions using pion spectra, elliptic flow, and femtoscopic radii

R. A. Soltz,^{*} I. Garishvili, M. Cheng,[†] B. Abelev, A. Glenn, J. Newby,[‡] and L. A. Linden Levy[§]
Lawrence Livermore National Laboratory
Livermore, California 94550

S. Pratt
Department of Physics and Astronomy and National Superconducting Cyclotron Laboratory,
Michigan State University
East Lansing, Michigan 48824
(Dated: June 15, 2022)

A new framework for evaluating hydrodynamic models of relativistic heavy ion collisions has been developed. This framework, a Comprehensive Heavy Ion Model Evaluation and Reporting Algorithm (CHIMERA) has been implemented by augmenting UVH 2+1D viscous hydrodynamic model with eccentricity fluctuations, pre-equilibrium flow, and the Ultra-relativistic Quantum Molecular Dynamic (UrQMD) hadronic cascade. A range of initial temperatures and shear viscosity to entropy ratios were evaluated for four initial profiles, N_{part} and N_{coll} scaling with and without pre-equilibrium flow. The model results were compared to pion spectra, elliptic flow, and femtoscopic radii from 200 GeV Au+Au collisions for the 0–20% centrality range. Two sets of initial density profiles, N_{part} scaling with pre-equilibrium flow and N_{coll} scaling without were shown to provide a consistent description of all three measurements.

I. INTRODUCTION

During the last decade a remarkable success has been achieved in the modeling and analysis of relativistic heavy ion collisions. Data from the Relativistic Heavy Ion Collider (RHIC) and more recently from the Large Hadron Collider (LHC) have surpassed the petabyte scale and include numerous classes of observables. The models that have been most successful in describing the soft physics observables of particle spectra and collective flow measured at RHIC (see [1–4] for a synopsis of the initial results) are those that incorporate relativistic hydrodynamics [5–7] coupled to a microscopic transport such as UrQMD [8, 9]. The relativistic hydrodynamic stage is used to describe the quark gluon plasma phase and its transition to hadronic matter, whereas the transport stage models the hadronic cascade which follows. Subsequent refinements to the hydrodynamic models to improve agreement with measured moments of the momentum anisotropy have incorporated shear viscosity [10, 11] and initial energy density fluctuations in the initial conditions [12–14]. The success of these models in reproducing the general features of particle spectra and elliptic flow have led to the conclusion that the QCD matter created in relativistic heavy ion collisions behaves very much like a fluid with small shear viscosity to entropy ratio.

Although the comparisons between models and data are both interesting and compelling, there is not yet a

complete and rigorous quantification of the uncertainties in the parameters that would describe the quark gluon plasma created in heavy ion collisions at RHIC and the LHC. The greatest uncertainty lies in our understanding of the initial, pre-thermalized state of the collision. Differences in the initial density profile that alter the hydrodynamic evolutions can lead to large uncertainties in the shear viscosity and initial temperature. The Equation of State (EoS) is calculated with increasing accuracy with lattice QCD [15, 16], but the interplay between the QCD EoS and the other parameters is yet to be explored. Furthermore, most model comparisons are often limited to a subset of measurements that are deemed most relevant to a specific line of inquiry. Some success in uncertainty quantification has been achieved by studying the relation between two observables, such as the ratio of elliptic flow to eccentricity and the multiplicity density [17]. However, a complete determination of the properties of matter created in heavy ion collisions will require a comprehensive comparison between a hybrid hydrodynamic model and a set of physics observables.

This paper describes a first step towards performing such a comparison, with the ultimate goal to fully constrain the properties of the quark gluon plasma. We have developed a Comprehensive Heavy Ion Model Evaluation and Reporting Algorithm (CHIMERA) for systematically comparing a set of hybrid hydrodynamic models for heavy ion collisions spanning a range of initial parameters. This framework enables one to determine the optimal parameters and associated uncertainties that best describe a set of soft physics measurements, incorporating both statistical and systematic errors. In the current implementation we use the 2D+1 viscous hydro code VH2 [10] augmented with initial state ec-

^{*} soltz@llnl.gov

[†] Present address: Boston University, Boston, MA 02215

[‡] Present address: Oak Ridge Nat. Lab., Oak Ridge, TN 37831

[§] Present address: MobiTV, Emeryville, CA 94608

centricity fluctuations [18] and pre-equilibrium flow [19] to describe the hydrodynamic evolution, and the Ultra-relativistic Quantum Molecular Dynamics hadronic cascade code (UrQMD) [8, 9] to describe the hadronic transport. Particle spectra and elliptic flow are generated from the UrQMD output, and femtoscopic correlations are produced by the Correlation After-Burner (CRAB) code [20, 21]. A chi-squared statistic is used to determine the best fit initial state parameters and associated uncertainties for the measured results and errors. For this paper, we compare to published spectra, elliptic flow, and femtoscopic correlations for pions measured by the STAR and PHENIX collaborations for $\sqrt{s_{NN}}=200$ GeV Au+Au collisions in the 0–20% centrality region.

In Section II we provide a detailed description of various components of the model, and in Section III we explain the procedures used to generate the model results and to evaluate the agreement with the data. The results of these evaluations are reported in Section IV and in Section V we give our conclusions and discuss future prospects and improvements.

II. THE MODEL

A. Initial Conditions and Hydrodynamic Evolution

The primary component of the model we employ is the freely available 2+1D viscous hydrodynamic code, VH2, developed by Luzum and Romatschke [10]. VH2 numerically solves the Muller-Israel-Stewart equations with finite shear viscosity in two dimensions assuming Bjorken boost invariant expansion along the longitudinal (beam) axis. We have modified the distributed version of VH2 in two ways: 1.) to account for effect of initial density on the average eccentricity for a given centrality, and 2.) to allow the initial state to be prepared with pre-equilibrium flow.

The standard version of VH2 determines the initial density profile by calculating the Glauber overlap integral for the Wood-Saxon density distributions of the colliding nuclei. The initial conditions are therefore smooth, and the density profile may be set by participant or binary collisions scaling. We have modified the calculation of the initial conditions to account for initial eccentricity fluctuations, using the TGlauber Monte Carlo method [22] with the default parameters $R=6.38$ fm, $a=0.535$, and a nucleon-nucleon cross-section $\sigma_{NN}=42$ mb. Smooth distributions were then obtained by averaging over 10,000 events, in which each event was rotated to align the participant or binary-collision reaction plane along the X-axis. An event sample of this size will still produce fluctuations in the tails of the distribution that the VH2 code is not designed to handle. In order to remove these fluctuations the portion of the distribution below 3% of the maximum was fit to a 2-D Gaussian in X and Y, which was then used to replace the initial distribution. As before, the initial density profile can be given by participant

scaling, binary collisions scaling, or a superposition of the two. In this paper we use both participant and binary scaling in order to bracket the range of initial density distributions with a Glauber model.

We have also introduced an option to prepare the initial state with pre-equilibrium flow. Vredevoogd and Pratt have shown that for a system with a traceless stress energy tensor that obeys Bjorken boost-invariant scaling and for which the anisotropy in the spatial components is largely independent of the spatial coordinates, the flow can be expressed as a universal function of the energy component and time [19],

$$\frac{T_{0x}}{T_{00}} \approx \frac{\partial_x T_{00}}{2T_{00}} t. \quad (1)$$

As implemented in this work, the individual fluid cells (0.2 GeV^{-1} on a side) are given initial transverse velocities according to Eq. 1 after the initial energy density distribution has been established. The addition of pre-equilibrium flow is expected to have the most impact on the elliptic flow and transverse radii. This can be seen in Fig. 1, where the upper panels show the evolution of the radial (left) and elliptic flow (right) through the mean transverse velocity and stress tensor asymmetry as a function of proper time. Radial and elliptic flow values are shown as a function of the proper time for start times of 0.6 fm/c (dotted) and 1.0 fm/c (solid). These are compared to VH2 run without pre-equilibrium flow for start times of 0.2 fm/c (double-dot-dashed), 0.6 fm/c (dot-dashed), and 1.0 fm/c (dashed). As the starting time is advanced, the systems that do not include pre-equilibrium flow begin to approximate the systems with pre-equilibrium flow, but they do not reach the same values. Advancing the start time without pre-equilibrium flow also advances the freeze-out time by a similar amount. Note that the two systems prepared with pre-equilibrium flow do not show much dependence on start time, a result that is consistent with the premise of a universal pre-equilibrium flow. The lower panels of Fig. 1 show the mean radial position and radial asymmetry for the same conditions. Again the earlier start times without pre-equilibrium flow approach, but do not match the values associated with pre-equilibrium flow, which show little dependence on start time. For the comparisons to experimental data that follow, we adopt a start time of 1.0 fm/c with and without inclusion of the pre-equilibrium flow. This start time is consistent with the choice in [10] for Glauber initial conditions.

The hydrodynamic evolution then precedes within the standard version of the VH2 code, using the QCD-inspired Equation of State based upon the work of Laine and Schroeder [23] to interpolate between the hadronic resonance model and the perturbative calculation. It provides a reasonable albeit imperfect approximation to the cross-over transition that is now calculated non-perturbatively using lattice QCD. A thorough study of the implications of various lattice calculations and their equation of state parameterizations is left for future in-

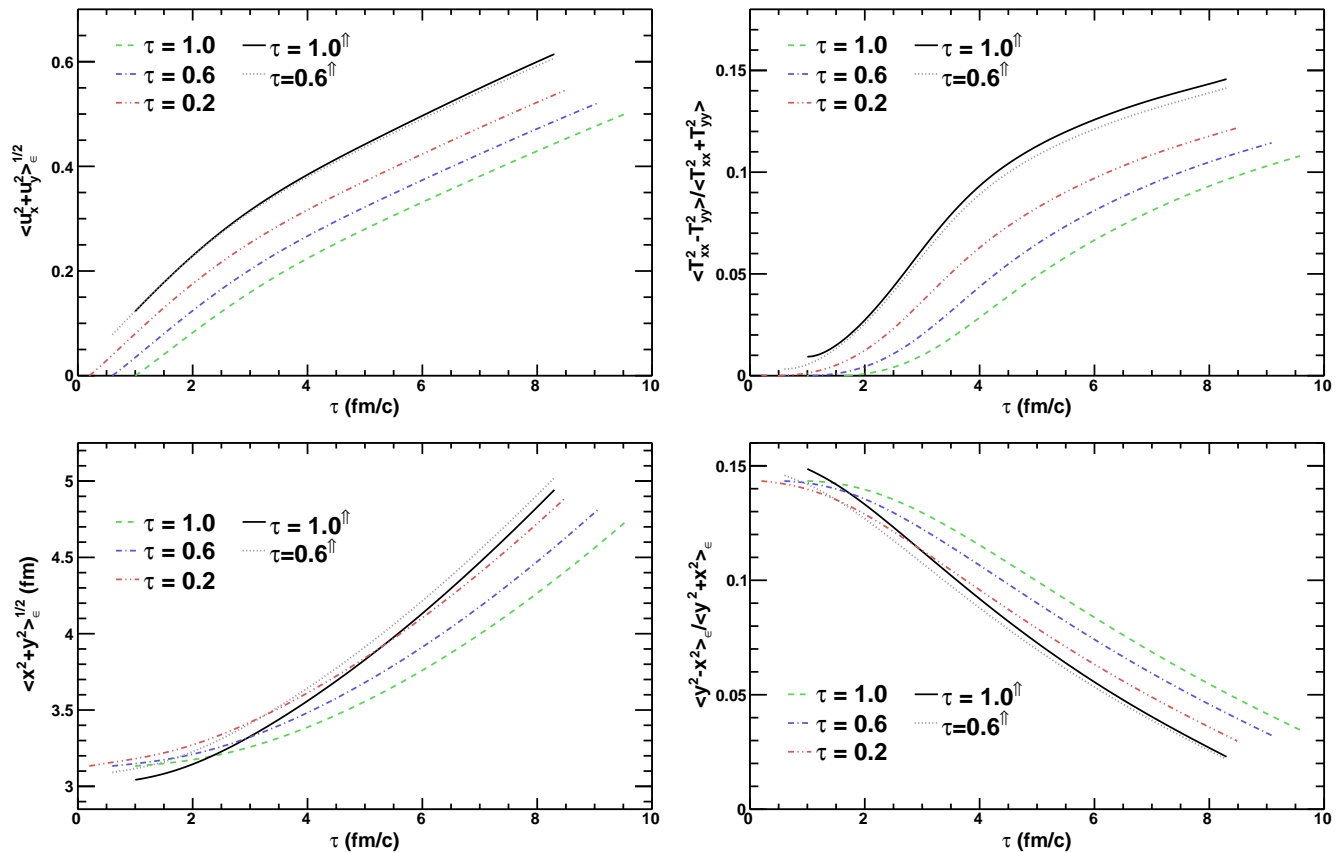


FIG. 1. The proper time evolution of mean radial velocity (upper left) and stress tensor asymmetry (upper right) flow for VH2 2+1D hydrodynamic evolution for Au+Au collisions with participant Glauber initial conditions for a $b = 4.4$ fm impact parameter and corresponding $b = 0$ initial temperature of 300 MeV. Contours are drawn for initial proper start times, $\tau=0.2, 0.6,$ and 1.0 fm/c without pre-equilibrium flow and for $\tau=0.6$ and 1.0 with pre-equilibrium flow as indicated in the legend by the \uparrow symbol. The mean transverse radial position (lower left) and eccentricity (lower right) are also shown. Note that all means are energy weighted.

vestigation.

B. Freeze-out and Hadronic Cascade

As in the standard version of VH2, the hydrodynamic evolution ceases when the temperature of a given cell falls below a specified freeze-out value. The final energy densities are converted to final state particles following the prescription of Cooper and Frye [24] with corrections for the shear viscosity implemented according to the method developed by Pratt and Torrieri [25]. In this method, the particle number and momentum distributions are determined by Monte Carlo sampling according to the non-viscous equilibrium distributions, and the momenta are subsequently rescaled according to Eq. 2,

$$p_j \rightarrow p_i + \lambda_{ij} p_j. \quad (2)$$

Here λ_{ij} is proportional to π_{ij} , the Israel-Stewart correction to the stress energy tensor. The constant of proportionality is chosen to reproduce the second order viscous

corrections to the final particle distributions for small values of π . The final state particles are selected to match the complete set of known particles used by the UrQMD code. For each hydro parameter set a file of 5000 events are generated using the OSCAR-97 format [26]. For comparisons to elliptic flow and radii, an additional 15000 particles are generated in order to achieve smaller statistical errors in the model results prior to fitting. We use a switching temperature of $T_{sw} = 165$ MeV to end the hydrodynamic evolution and generate the particles for the subsequent hadronic cascade stage of the model. As in [11], this value of T_{sw} was chosen to be as close as possible to, but still larger than the transition temperature. The freeze-out particle times are converted to formation times and the particles are back-propagated to zero time using the standard *oscar2u* program provided by the UrQMD developers upon request.

For this paper we use UrQMD v2.3 to model particle interactions that follow the hydrodynamic freeze-out stage. UrQMD is run with default switches except modifications needed to read the OSCAR-97 formatted in-

put file. We also disable the unstable particle decay after the final time step, in order to allow for comparison to the full set of particle spectra measured and reconstructed by the experiments. The CHIMERA framework can also be used without the hadronic cascade. In this case, the list of final state particles is taken from the list of stable particles from the 2008 listing of the Particle Data Group [27] and a lower freeze-out temperature $T_{sw}=140$ MeV is used.

C. Post Processing

The final state particle distributions from UrQMD are then used to construct the observables that can be directly compared to published experimental data. In this work we restrict our comparison to invariant particle spectra, the second coefficient of the transverse momentum anisotropy with respect to the event reaction plane v_2 , and the Bertsch-Pratt femtoscopic radii, R_{long} , R_{side} , R_{out} . The transverse momentum spectra are calculated as invariant cross-sections using bins of 0.1 GeV/c in the range 0.2–1.5 GeV/c and rapidity interval of $|y| < 0.5$. The elliptic flow is calculated within the same transverse momentum region. We use CRAB to generate the three-dimensional femtoscopic correlation functions, including the strong interaction and statistical interference. The Coulomb interaction is neglected so that a 3D Gaussian can be used to fit the correlation function to generate the radii. The correlation functions are also binned in 0.2 GeV intervals. The fits are performed directly on the correlation weights, to avoid the time and cpu-consuming process of constructing an event mixed background for each momentum bin.

The cumulative effect of each modification to the VH2 code is shown in Figs. 2 and 3. Fig. 2 shows the charged particle yields and mean transverse momentum ($\langle p_T \rangle$) for pions (filled triangles), kaons (filled inverse triangles), and protons (open triangles). The unmodified VH2 results are shown as solid circles with connecting lines, and correspond to a binary scaling optical Glauber model input for an initial central temperature of $T_{cent} = 333$ MeV, $\eta/s = 0.08$ and a freeze-out temperature of 140 MeV. These parameters were chosen to match the upper panels of Fig. 7 of [28]. Here we follow the VH2 convention in reporting the equivalent temperature, T_{cent} , for a central collision (zero impact parameter). As in [28], the model results are compared to PHENIX measurements from [29]. The results in Fig. 2 make use a different freeze-out routine, described above, that was written to accommodate the need to write OSCAR formatted events for input to CRAB and UrQMD. Therefore the results may differ slightly from the published VH2 results. We then add, in succession, eccentricity fluctuations (open circles), pre-equilibrium flow (open squares) and UrQMD with a switching temperature of $T_{sw} = 165$ MeV (filled squares). The incorporation of the eccentricity fluctuations has only small im-

pact on the particle yields and $\langle p_T \rangle$, but the addition of pre-equilibrium raises the $\langle p_T \rangle$ by as much as 20%. The hadronic cascade phase leads to increased proton yields and decreased $\langle p_T \rangle$ for pions and kaons; both can result from collisions in UrQMD involving baryonic resonances. In adding features to the model, we make no attempt to modify the initial parameters to achieve better agreement with the data. This will be the main focus of the results section.

Similar comparisons for the elliptic flow for charged hadrons and sideways and outwards radii for pions are shown in Fig. 3. Each modification to VH2 serves to increase the v_2 . For $N_{part} < 200$ the model results come closer to the comparison data measured by STAR [3], however for more peripheral collisions the addition of pre-equilibrium flow causes the value of v_2 to overshoot the data. It may be that for very peripheral collisions the anisotropy of the stress energy tensor may no longer be independent of the spatial coordinates, thereby violating the conditions required for universal flow [19]. The hadronic cascade phase leads to a reduction in the value of v_2 , when compared to a pure hydrodynamic evolution with lower freeze-out temperature.

The right panel of Fig. 3 shows the cumulative effects on the transverse radii, R_{out} and R_{side} . Note that each modification leads to a reduction in R_{out} and an increase in R_{side} , bringing the two closer to each other and to the ratio observed in the data. The measurements by STAR and PHENIX for 200 GeV Au+Au are omitted from this figure for clarity in order to better reveal the trends, which are consistent with the one-dimensional relativistic viscous hydro results documented in [30].

III. MODEL EVALUATION

A. Model Parameterizations

Because the published experimental results do not generally conform to a uniform binning, the model results are fit to a functional form prior to evaluating the overall agreement with the data. This step also simplifies the treatment of systematic errors in the data. We selected a purely empirical fitting function in order to avoid an bias in treating the model results prior to comparison to experiment. To describe the p_T dependence of v_2 and the k_T dependence of the femtoscopic radii we fit a third order Chebyshev polynomial to these data. However, polynomials are not easily adapted to the large dynamic range characteristic of spectra. For the spectra one needs an exponential form to describe the data, and we achieved good agreement by multiplying a fifth order Chebyshev polynomial by an exponential in transverse mass that has been shown to fit a wide range of particle spectra [29]. The functional form used to fit the model spectra is given

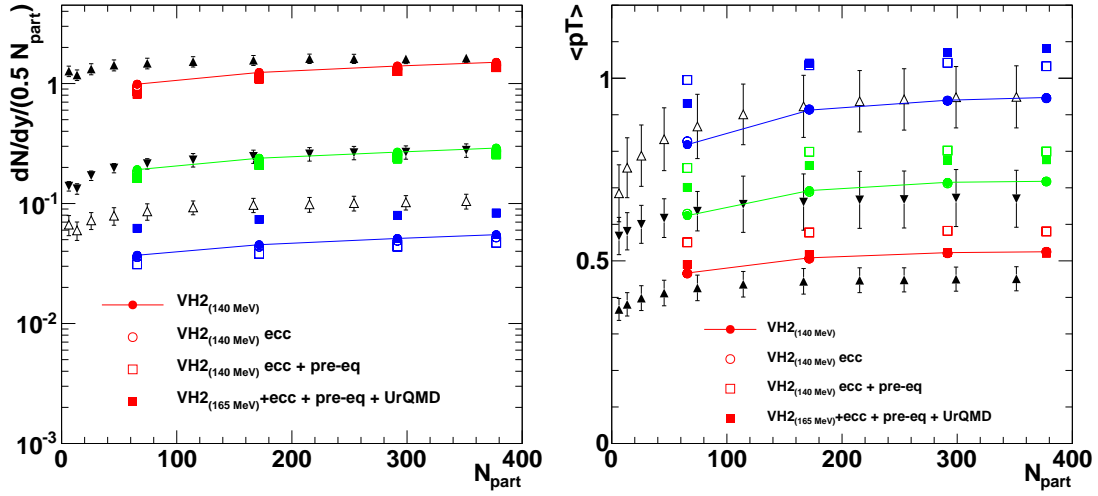


FIG. 2. dN/dy (left) and mean transverse momenta (right) for pions (red), kaons (green), and protons (blue) for the unmodified VH2 (solid connected circles), and for the cumulative effect of adding eccentricity fluctuations (open circles), pre-equilibrium flow (open squares) and switching to the UrQMD hadronic cascade (solid squares) at $T_{sw} = 165$ MeV. Model results are compared to PHENIX measurements for pions (filled triangles), kaons (inverted filled triangles), and protons (open triangles). In this figure the open-circle symbols for the eccentricity fluctuations are often obscured by filled-circle results from the unmodified VH2 results.

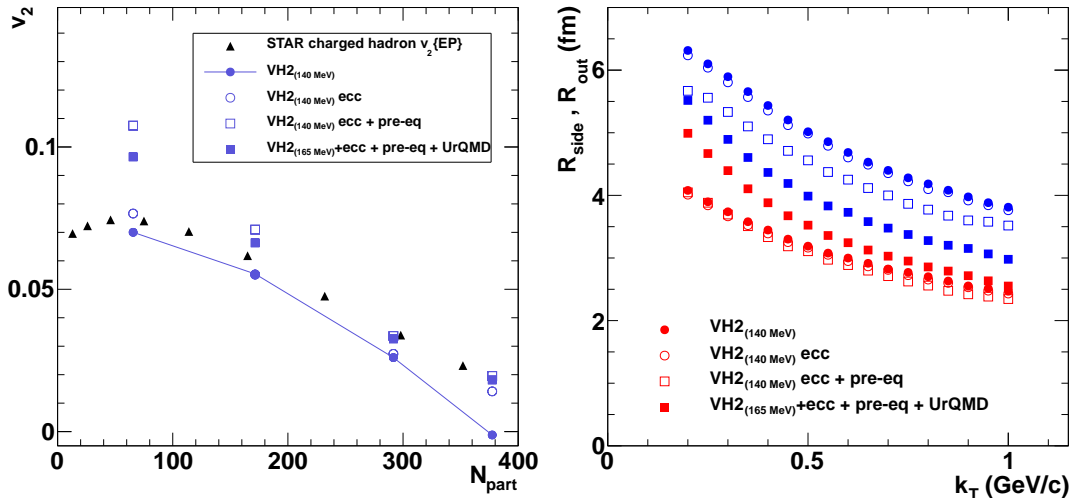


FIG. 3. Mean elliptic flow for VH2, adding eccentricity fluctuations, pre-equilibrium flow, and the UrQMD cascade after-burner (left). R_{side} and R_{out} femtoscopic radii for the same conditions (right).

by Eq. 3,

$$y(p_T) = \left(\sum_{i=1}^5 a_i T_i(p_T) \right) \cdot \frac{\exp[-(m_T - m_0)/T]}{2\pi T(T + m_0)} \quad (3)$$

We count on the Chebyshev multiplier to cancel any bias that may result from incorporating the slope parameter, T , into the fit. We have verified that these functional forms provide a good description of the model results, with χ/dof close to unity for most systems.

B. Data Comparisons

To evaluate the model parameters we calculate a chi-squared statistic for each combination of model parameterization and data set. We have selected four different initial states for evaluation, including both participant (N_{part}) and binary collision (N_{coll}) scaled energy density profiles, each prepared with and without pre-equilibrium flow. The initial Glauber distributions were generated for a fixed impact parameter of 4.4 fm, corresponding to the 0–20% centrality bin for 200 GeV Au+Au collisions. The initial viscosity to entropy ratios were sampled in steps of

0.08, from a lower bound of 0.001 (a non-zero value is required for numerical stability) to an upper bound of 0.48. The temperature was varied in steps of 5 MeV for spectra and 20 MeV for flow and radii, with the ranges adjusted iteratively to reach above and below the optimal parameter values for each set of initial conditions. The full set of input parameters and data comparison sets are listed in Table I. The centrality range of 0–20% was selected to

Initial Profile	η/s	$T_{cent}^{spectrum}$	$T_{cent}^{v2-femto}$
N_{part}	0.001–0.48	280–325 MeV	260–380 MeV
N_{part} pre-eq. flow	0.001–0.48	270–315 MeV	260–380 MeV
N_{coll}	0.001–0.48	330–370 MeV	300–420 MeV
N_{coll} pre-eq. flow	0.001–0.48	310–350 MeV	300–420 MeV

TABLE I. Initial VH2 density profile and range of central temperatures (T_{cent}) and η/s values. All runs used a fixed 4.4 fm impact parameter with $\langle N_{part} \rangle = 276$, $\tau = 1.0$ fm/c, the default QCD-inspired EOS, and $T_{sw} = 165$ MeV.

avoid large corrections to the v_2 associated with non-flow effects in the data [31] and to match existing pion femtoscopia, v_2 , and spectra. The pion spectra are compared to the 0–20% centrality measurements by PHENIX [29] and STAR [32]. CHIMERA matches models to data by their centrality using $\langle N_{part} \rangle$. For this impact parameter we calculate a value of $\langle N_{part} \rangle = 276$, whereas PHENIX reports a value of 286 and STAR reports a value of 282. The nearest pion radii for PHENIX are for the centrality range of 0–30%, but the presence of two pions in one of the PHENIX central arms imposes a slight centrality bias and $\langle N_{part} \rangle = 281$ for these data [33]. The nearest centrality bin for the STAR pion radii is 5–10%, which have $\langle N_{part} \rangle = 298$ [34]. Based on the N_{part} scaling analysis in [35], this leads to a difference in radii of less than 2%, well below the errors of either measurement. For the v_2 we compare to two sets of measurements by PHENIX in this centrality range, a combined analysis of pions and kaons [36], and a recent analysis of pion v_2 at higher p_T [37]. The STAR v_2 results for pions are also from the 5–10% centrality range [3]. From the centrality dependence shown in Fig. 3, the difference in v_2 for a change of 14 in $\langle N_{part} \rangle$ is close to 5%, which is comparable to the reported errors and may be large enough to influence the results.

To incorporate the systematic errors when evaluating the chi-squared statistic, we follow the procedure defined in [38]. Because it is generally not feasible to calculate a full co-variance matrix for the systematic errors, the authors of [38] make a set of simplifying assumptions that correspond to different types of systematic errors. For this analysis we assume all systematic errors assumed to be of type B, in which the systematic errors are assumed to be fully correlated in the fractional deviation. With this assumption, the modified χ^2 formula reduces to,

$$\chi^2(\epsilon_b, p) = \left[\left(\sum_{i=1}^n \frac{(y_i + \sigma_{b_i} - \mu_i(p))^2}{\sigma_i^2 (1 + \epsilon_b \sigma_{b_i} / y_i)^2} \right) + \epsilon_b^2 \right], \quad (4)$$

where σ_{b_i} represents the systematic error, and ϵ_b represents the fraction of the error by which the set of correlated measurements move in tandem. The full procedure for evaluating the modified χ^2 and the derivation are given in the appendix of [38].

IV. RESULTS

The CHIMERA model comparison results are shown in Figs. 4–15. For each of these figures, the leftmost panel shows the result with fixed η/s set to the conjectured minimum value of 0.08. The middle panel shows the variation with η/s for fixed temperature, set to the approximate minimum. The Chebyshev fits to the model results are shown and the experimental data are plotted with both statistical error bars and systematic error boxes. The calculated values of χ_{dof}^2 are reported separately for each experiment. Because the wide dynamic range of the spectra can obscure subtle differences, the ratios of data to model fits are also shown. The upper rightmost panel shows the sum of the χ^2 over all data sets divided by the total degrees of freedom (dof). Paraboloid fit to the χ_{dof}^2 distribution is shown below. The paraboloid fits to the χ_{dof}^2 distributions will be used to extract confidence contours for each measurement.

Fig. 4 shows the model fits, data, and χ_{dof}^2 distribution for the pion spectra from N_{part} scaling without pre-equilibrium flow. In general, the calculated spectra are harder (less steep) than the data, a condition that will persist for the other initial conditions. The spectra harden further with increasing η/s , a feature evident in [10] but not often shown due to the propensity to use the spectra to constrain only the temperature. However, this establishes an inverse correlation between χ_{dof}^2 minima in T and η/s , as shown in the right panel of Fig. 4.

In Fig. 5 one can see that the addition of pre-equilibrium flow serves to further harden the spectra. Some flexibility to find a reasonable χ_{dof}^2 minimum is provided by the freedom for the lower p_T spectra from STAR to move independently from the PHENIX data, each within their systematic errors. However, the curvature for the χ_{dof}^2 distribution is noticeably steeper. The parameters for the paraboloid fits to these and all other measurements are listed in Table II.

The model comparisons for the N_{coll} scaling are shown in Fig. 6. The N_{coll} scaling results require a higher temperature to match the pion multiplicity, which further exacerbates the difference in slope. When the pre-equilibrium flow is added in Fig. 7, the agreement with data is poorer. The χ_{dof}^2 values for the minima are significantly higher and the distribution is quite steep.

Figs. 8 and 9 show the model evaluations for the elliptic flow, with the absence and addition of pre-equilibrium flow, respectively. Comparisons are shown separately for pions from STAR and PHENIX, and earlier results from PHENIX that combine pions and kaons. Without pre-equilibrium, the minimum occurs near zero η/s and at

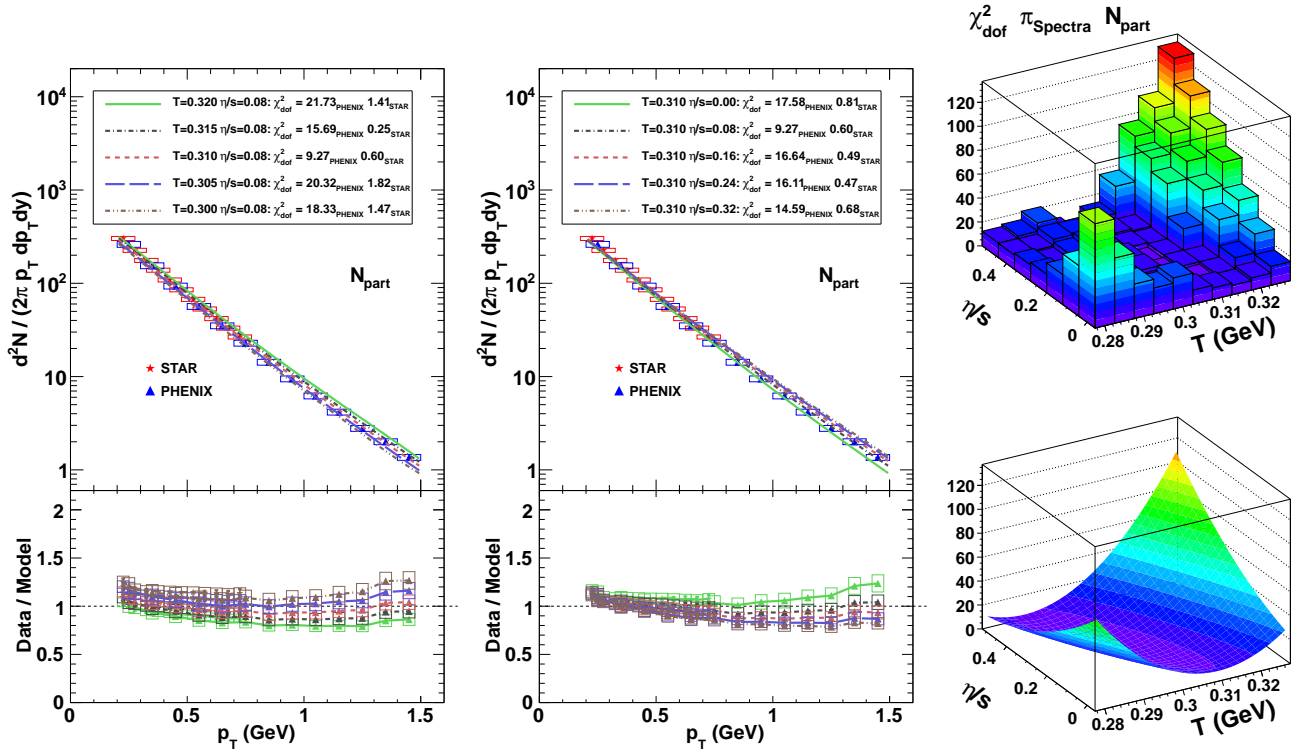


FIG. 4. Model evaluation of pion spectra with N_{part} scaling for fixed T (left), fixed η/s (middle), with total χ^2_{dof} distribution (upper right) with paraboloid fit (lower right).

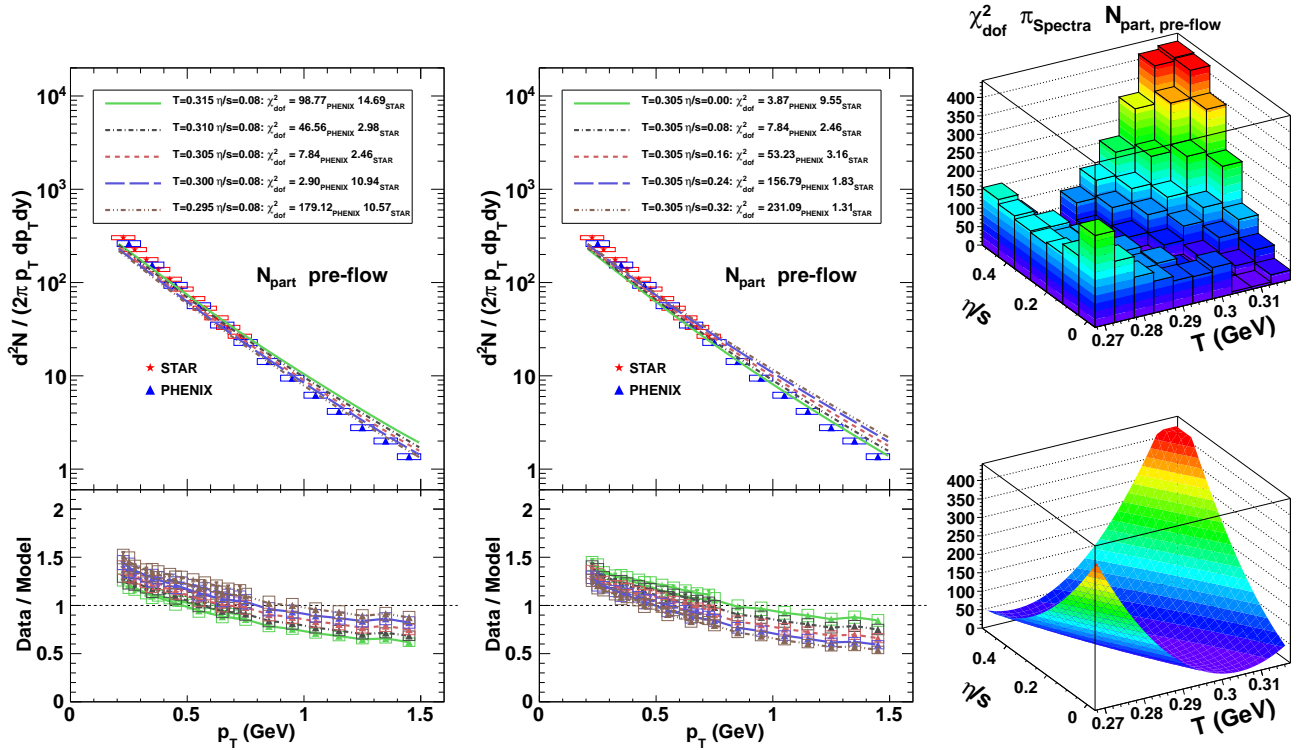


FIG. 5. Model evaluation of pion spectra with N_{part} scaling and pre-equilibrium flow for fixed T (left), fixed η/s (middle), with total χ^2_{dof} distribution (upper right) with paraboloid fit (lower right).

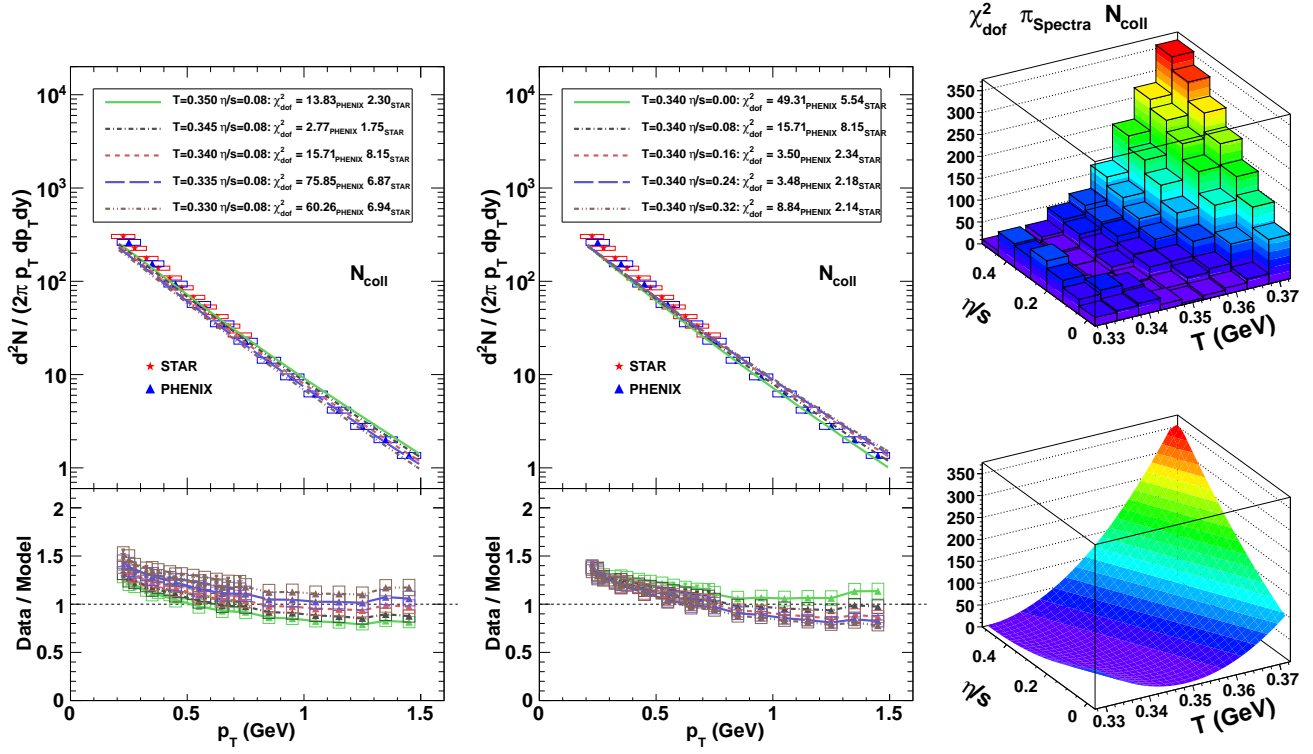


FIG. 6. Model evaluation of pion spectra with N_{coll} scaling for fixed T (left), fixed η/s (middle), with total χ^2_{dof} distribution (upper right) with paraboloid fit (lower right).

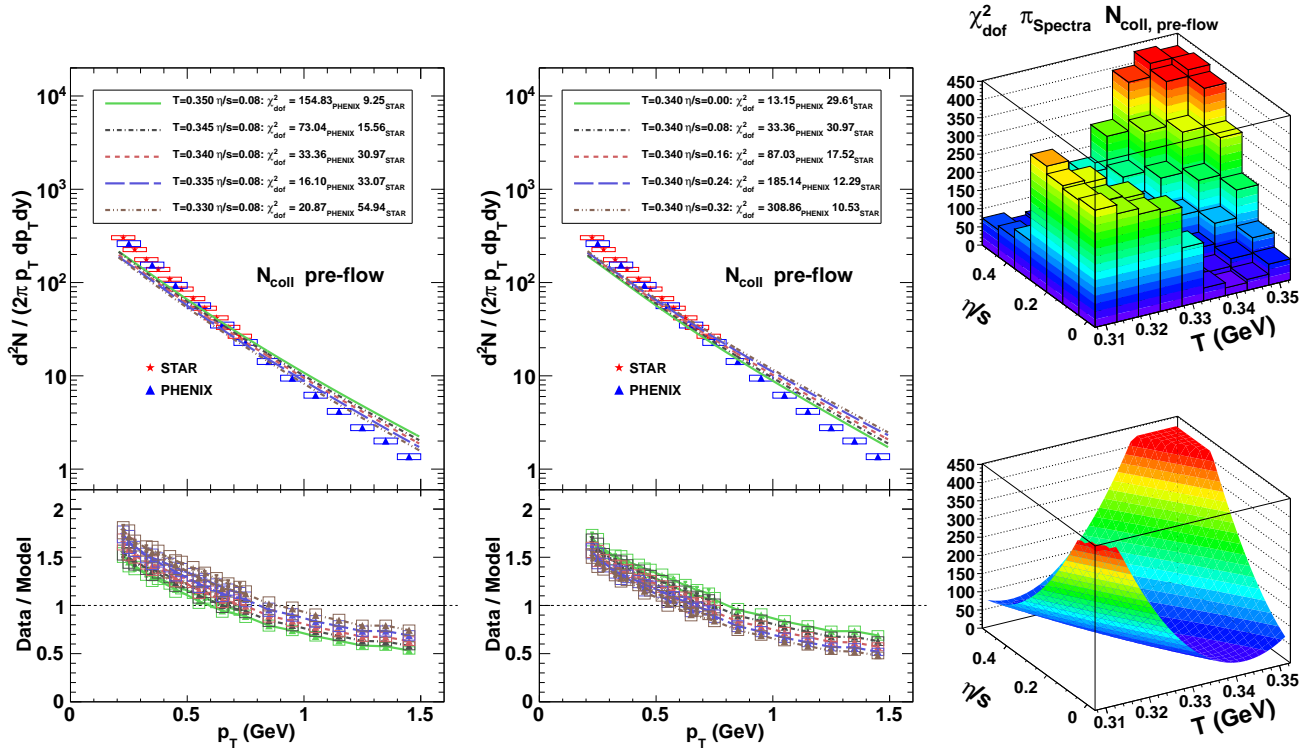


FIG. 7. Model evaluation of pion spectra with N_{coll} scaling with pre-equilibrium flow for fixed T (left), fixed η/s (middle), with total χ^2_{dof} distribution (upper right) with paraboloid fit (lower right).

Initial profile	Evaluation	Major axis	Minor axis	angle (deg)	T_{\min}	η/s_{\min}	χ^2/dof_{\min}
N_{part}	HBT	0.211	0.0114	0.282	0.266	0.5	13.9
	V_2	0.0884	0.0134	6.52	0.347	0.001	11.5
	Spectra	0.153	0.00379	2.3	0.297	0.286	2.67
	Sum	0.126	0.00489	2.18	0.297	0.222	12.7
	Sum ₁₀	0.127	0.00744	1.24	0.293	0.207	19.2
N_{coll}	HBT	0.237	0.0121	1.01	0.317	0.52	14.1
	V_2	279	0.0318	19.2	0.324	0.117	3.94
	Spectra	210	0.0023	2.27	0.348	0.001	4.44
	Sum	620	0.00323	2.15	0.341	0.175	10.6
	Sum ₁₀	13.8	0.00678	2.01	0.334	0.277	14.4
$N_{part}^{pre-flow}$	HBT	0.374	0.0105	2.51	0.273	0.52	4.81
	V_2	0.335	0.0393	14.2	0.322	0.001	4.8
	Spectra	0.0938	0.00185	3.11	0.303	0.001	4.88
	Sum	0.128	0.00271	2.96	0.302	0.001	6.29
	Sum ₁₀	0.246	0.00587	2.69	0.3	0.001	6.38
$N_{coll}^{pre-flow}$	HBT	0.434	0.013	2.52	0.361	0.237	4.34
	V_2	0.156	0.0552	19.3	0.29	0.299	3.53
	Spectra	0.0855	0.00147	3.05	0.341	0.001	29.8
	Sum	0.138	0.00218	3.05	0.341	0.001	18
	Sum ₁₀	0.182	0.005	2.91	0.328	0.256	8.38

TABLE II. Ellipse parameters determined from paraboloid fits to χ_{dof}^2 distributions in T and η/s for each set of initial condition profile and for each measurement.

higher values of the temperature. With the addition of pre-equilibrium flow higher values of η/s and lower temperatures can be accommodated. In contrast to the model comparisons for spectra, the χ_{dof}^2 distributions for v_2 evaluations exhibit more fluctuations, a sign that the model statistics can be further improved if more events are generated.

The elliptic flow comparisons for N_{coll} scaling are shown in Fig. 10. The larger pressure gradients of the N_{coll} scaling push the minima to higher η/s values, into a region of $1 < 4\pi\eta/s < 2$, consistent with the initial VH2 results using Glauber N_{coll} geometry [10] and the recent work of Song *et al.* [17]. The addition of pre-equilibrium flow shown in Fig. 11 pushes this minimum even higher. However, the χ_{dof}^2 distributions are quite broad. Aside from the exclusion of the high T , η/s region without pre-equilibrium flow and the low η/s region when pre-equilibrium flow is added, there appears to be limited constraining power from comparing to the p_T dependence of one particle species at a single centrality.

In Fig. 12 we show for the first time a direct comparison of VH2+UrQMD values of R_{long} , R_{side} , and R_{out} compared to experimental data for 200 GeV Au+Au collisions. The comparison displays the characteristic discrepancy (referred to as the HBT puzzle [39]) in which R_{out} trends above the data and R_{side} trends below. Better agreement is obtained for lower temperatures, where a minimum value of χ_{dof}^2 below 20 is achieved in the $T=260$ MeV bin. However, this is also below the tem-

perature constraints set by the spectra. When pre-equilibrium flow is added, as shown in Fig. 13, the overall agreement improves significantly, and the χ_{dof}^2 minimum occurs at temperature of 320 MeV, within the range of values allowed by the spectra. The femtoscopic radii have little to no constraining power on the shear viscosity.

The model evaluation for N_{coll} scaling pion radii results shown in Fig. 14 are similar in feature to the N_{part} scaling results. The χ_{dof}^2 minimum is shifted to higher temperature, but by an amount similar to the magnitude of the shift that occurs for the spectra. Fig. 15 shows the agreement improving again with the addition of pre-equilibrium flow.

Before we return to examine the similarities and differences among the constraints obtained from each measurement, we construct the ratio of the sum of all χ^2 to the sum of all degrees of freedom for each set of initial conditions to explore whether it is feasible to obtain an overall constraint on T and η/s . These distributions are shown in Fig. 16 for the full set of initial profiles and pre-equilibrium conditions. These distributions do not differ from the χ_{dof}^2 distributions for the spectra alone, shown in Figs. 4–7. This is also readily seen in Table II, in which the locations of the χ_{dof}^2 minima are identical for both initial profiles with pre-equilibrium flow, and for the N_{part} scaling. For the N_{coll} scaling, the location of the minimum in η/s moves to the higher η/s value determined from the elliptic flow evaluation.

The decision to construct an equal weight sum was

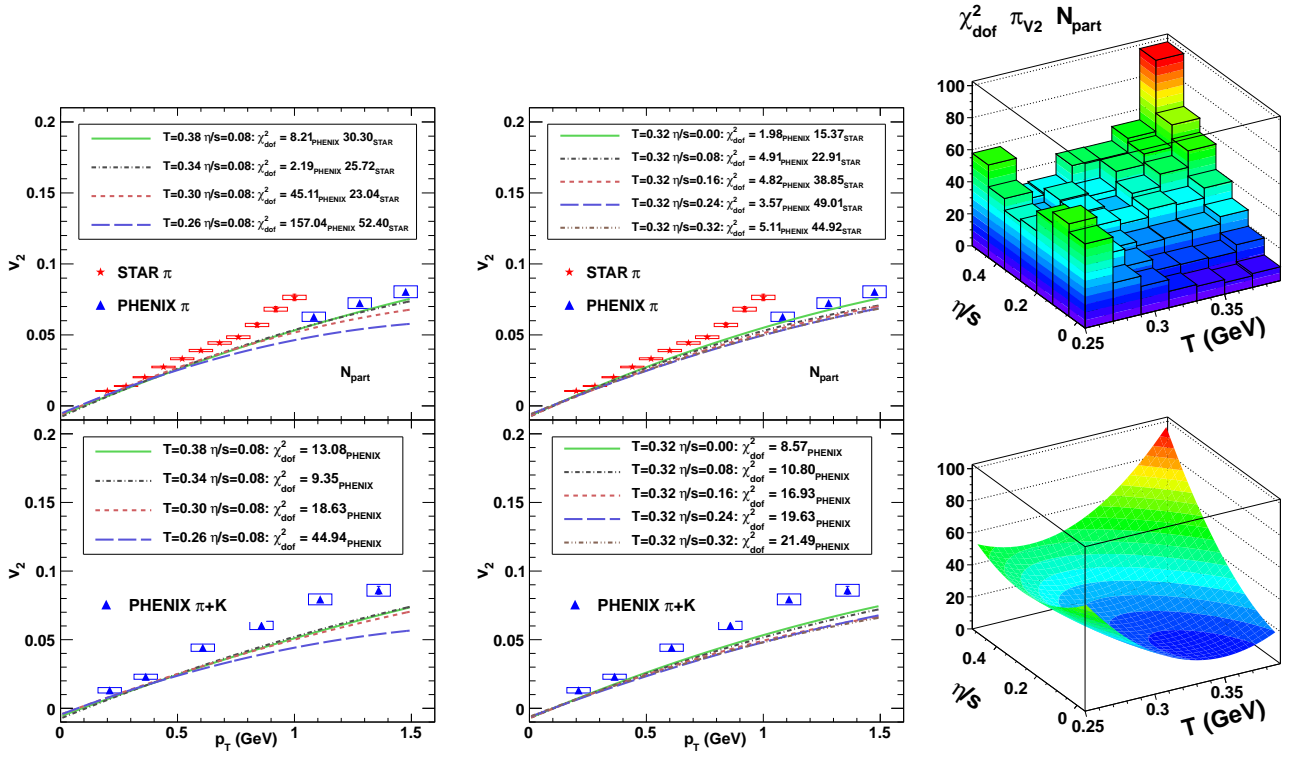


FIG. 8. Model evaluation of pion elliptic flow with N_{part} scaling for fixed T (left), fixed η/s (middle), with total χ^2_{dof} distribution (upper right) with paraboloid fit (lower right).

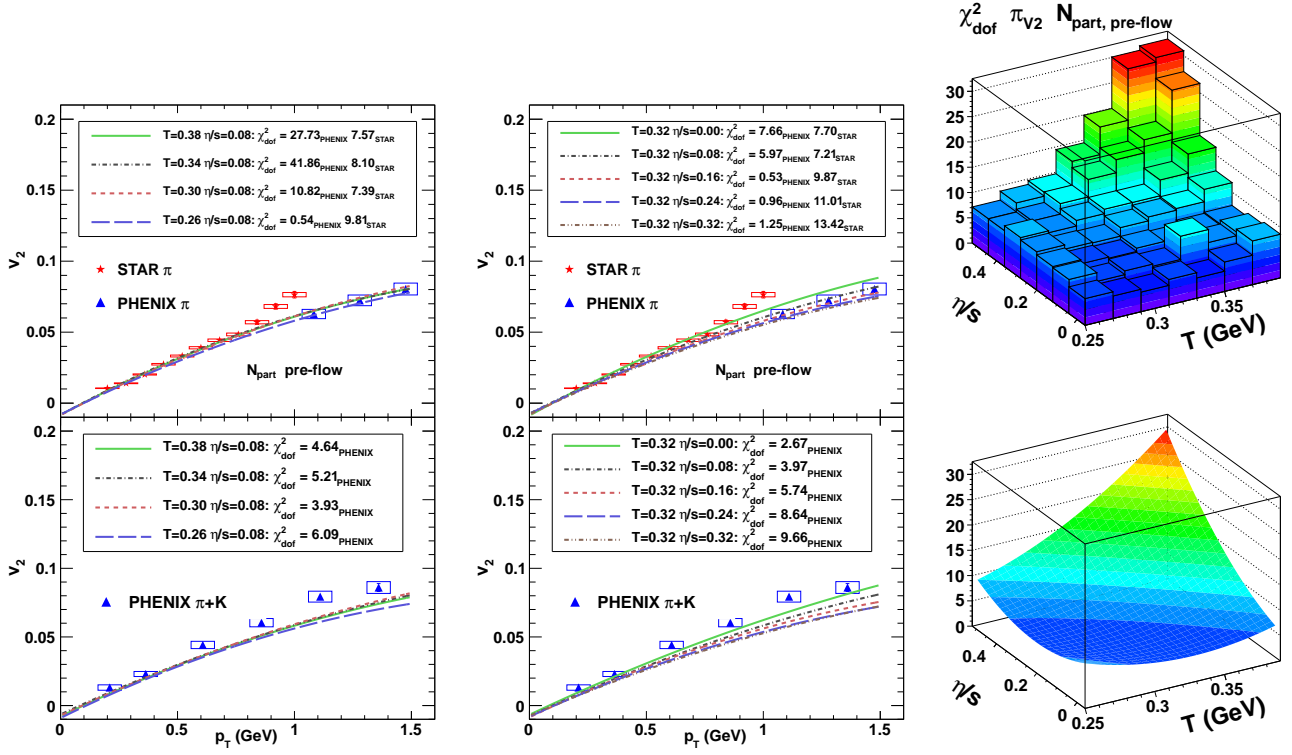


FIG. 9. Model evaluation of pion elliptic flow with N_{part} scaling with pre-equilibrium flow for fixed T (left), fixed η/s (middle), with total χ^2_{dof} distribution (upper right) with paraboloid fit (lower right).

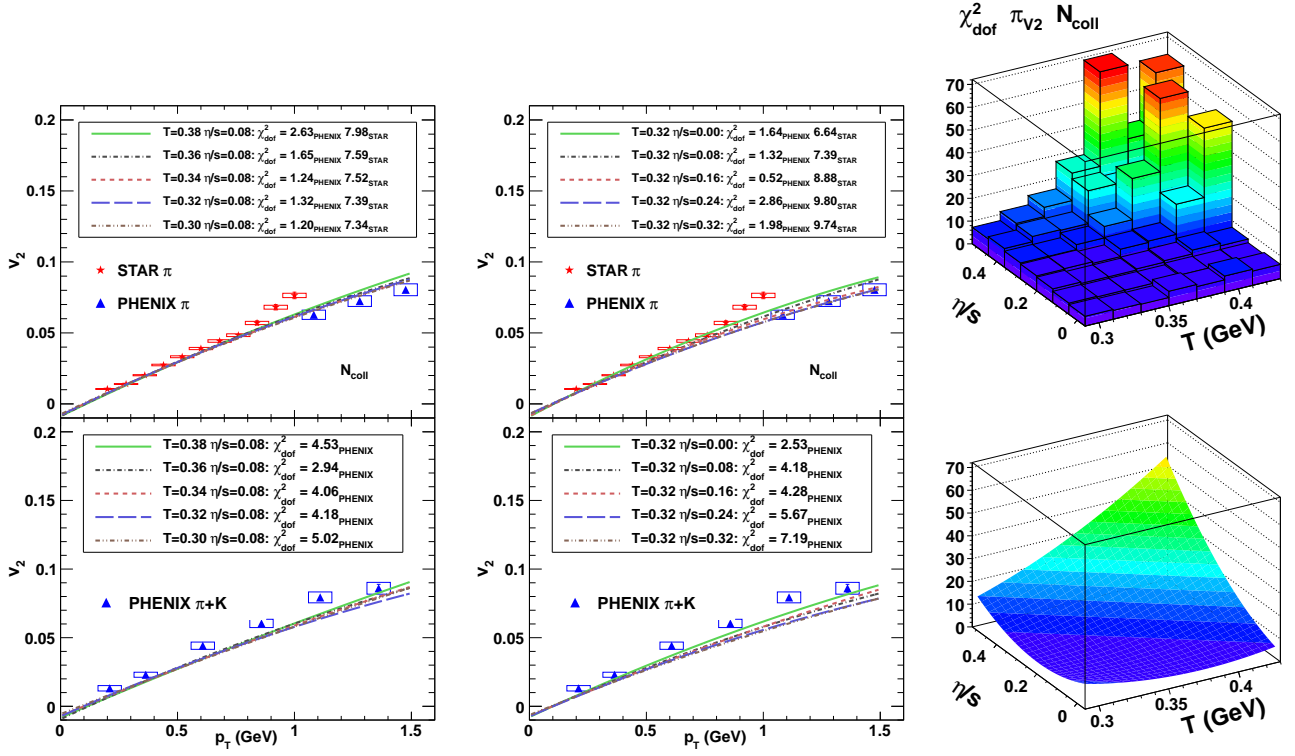


FIG. 10. Model evaluation of pion elliptic flow with N_{coll} scaling for fixed T (left), fixed η/s (middle), with total χ_{dof}^2 distribution (upper right) with paraboloid fit (lower right).

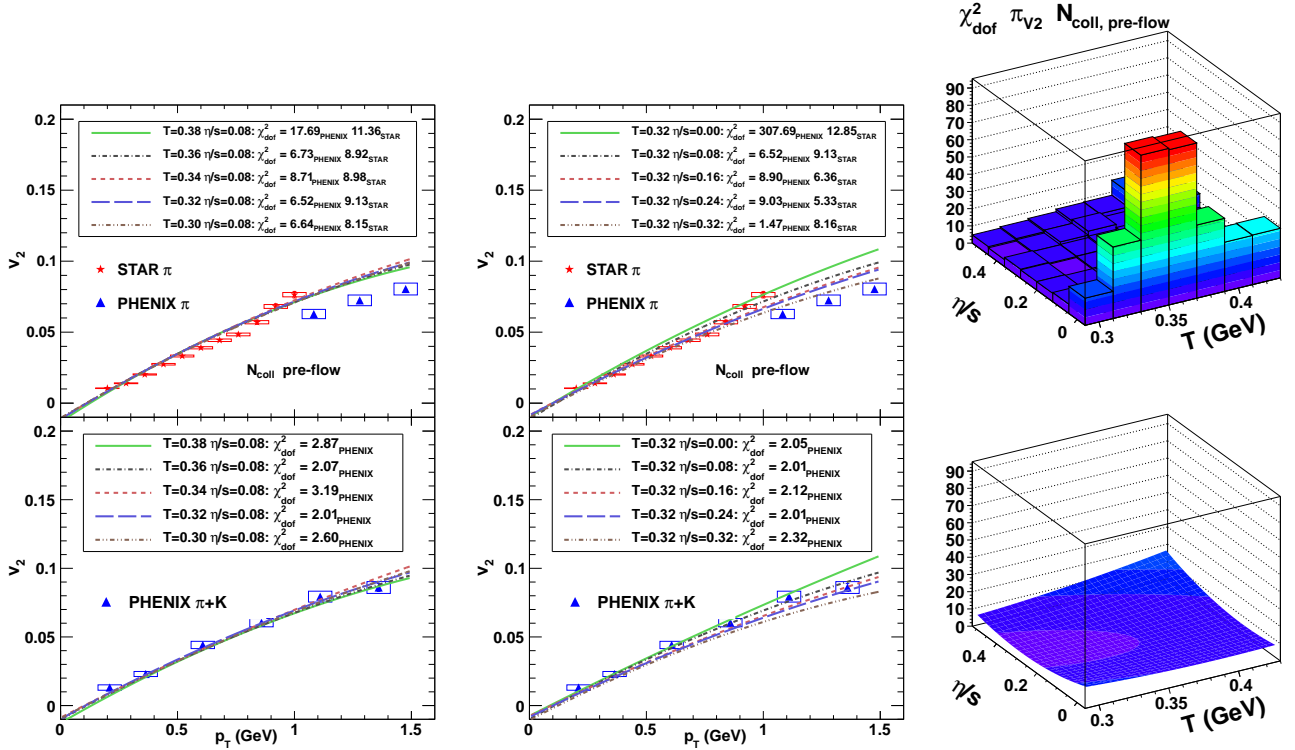


FIG. 11. Model evaluation of pion elliptic flow with N_{coll} scaling with pre-equilibrium flow for fixed T (left), fixed η/s (middle), with total χ_{dof}^2 distribution (upper right) with paraboloid fit (lower right).

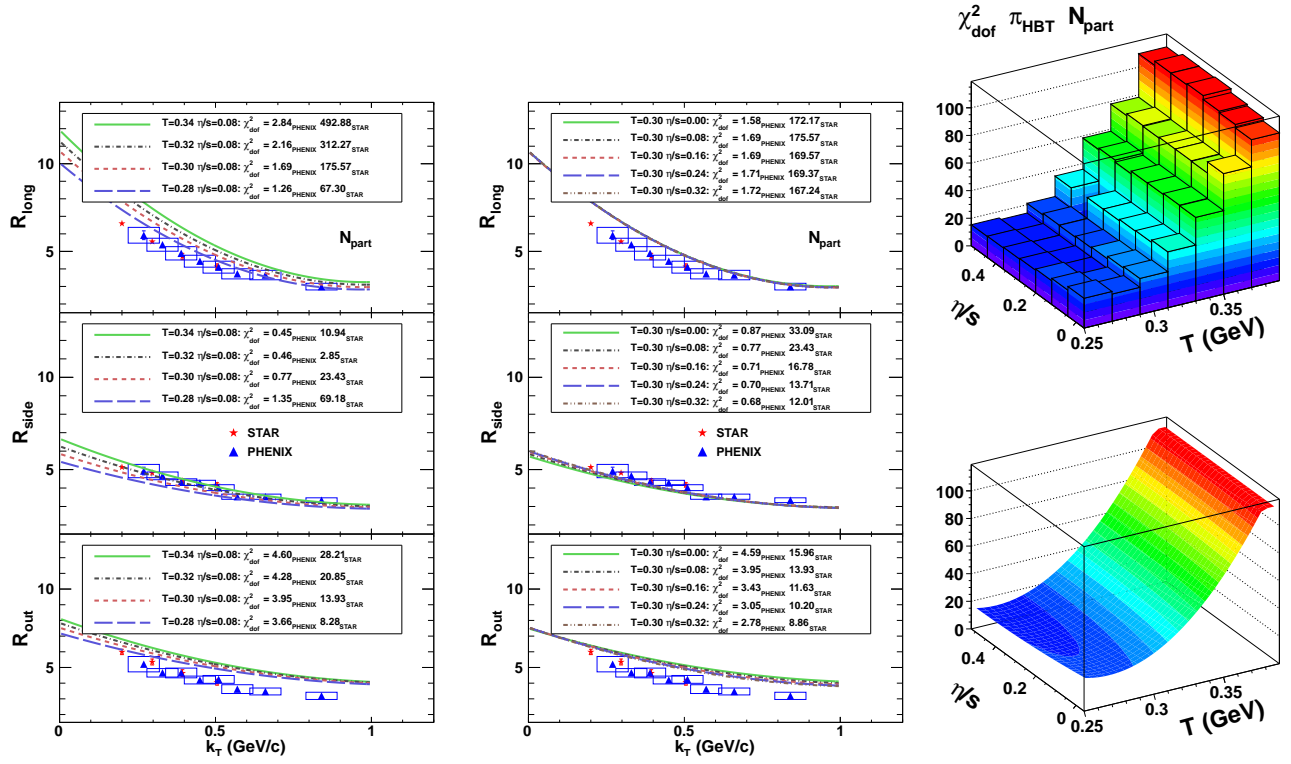


FIG. 12. Model evaluation of pion radii with N_{part} scaling for fixed T (left), fixed η/s (middle), with total χ^2_{dof} distribution (upper right) with paraboloid fit (lower right).

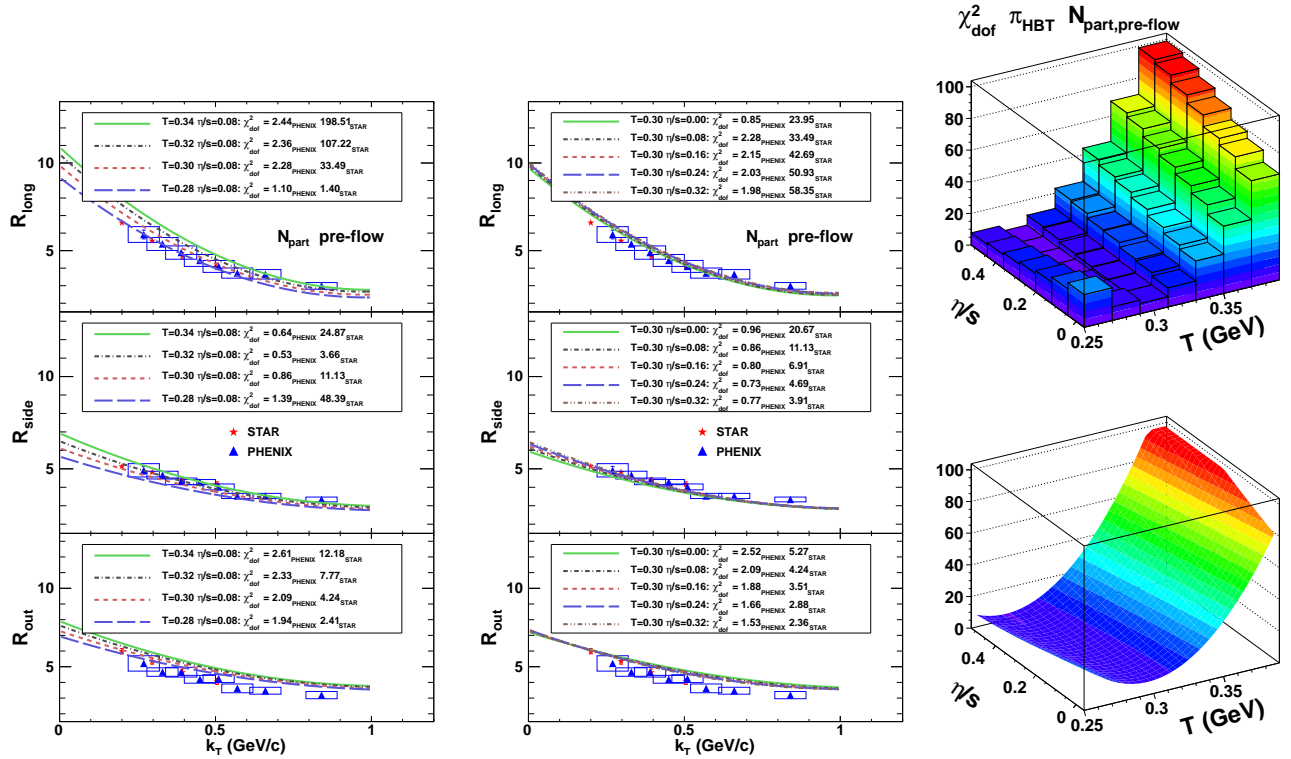


FIG. 13. Model evaluation of pion radii with N_{part} scaling with pre-equilibrium flow for fixed T (left), fixed η/s (middle), with total χ^2_{dof} distribution (upper right) with paraboloid fit (lower right).

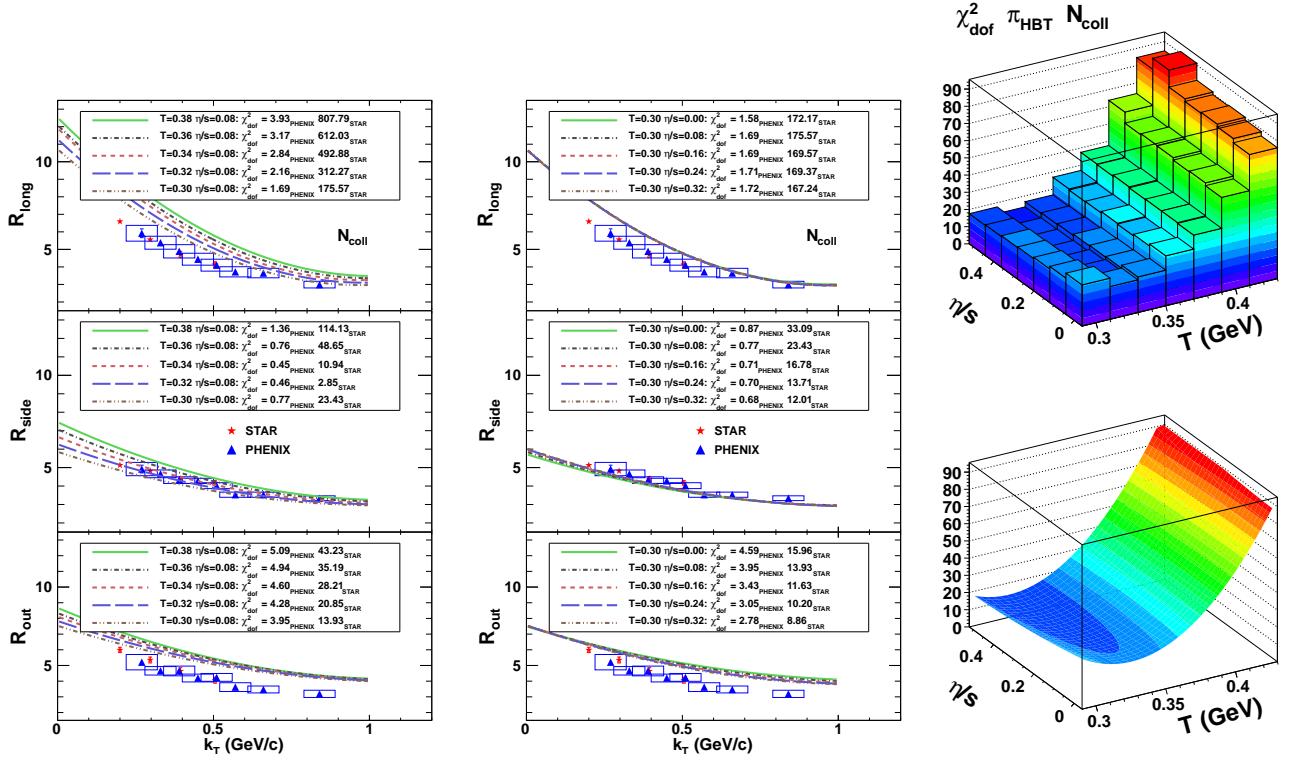


FIG. 14. Model evaluation of pion radii with N_{coll} scaling for fixed T (left), fixed η/s (middle), with total χ^2_{dof} distribution (upper right) with paraboloid fit (lower right).

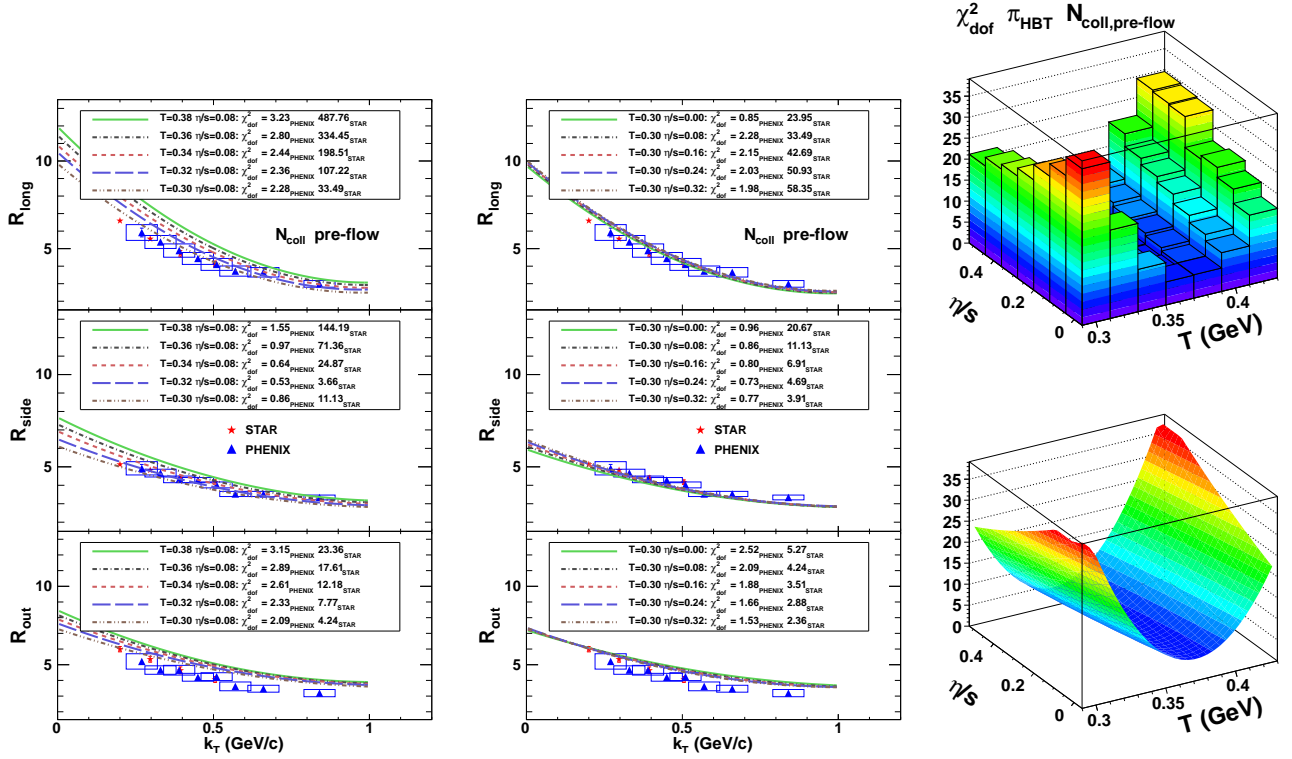


FIG. 15. Model evaluation of pion radii with N_{coll} scaling with pre-equilibrium flow for fixed T (left), fixed η/s (middle), with total χ^2_{dof} distribution (upper right) with paraboloid fit (lower right).

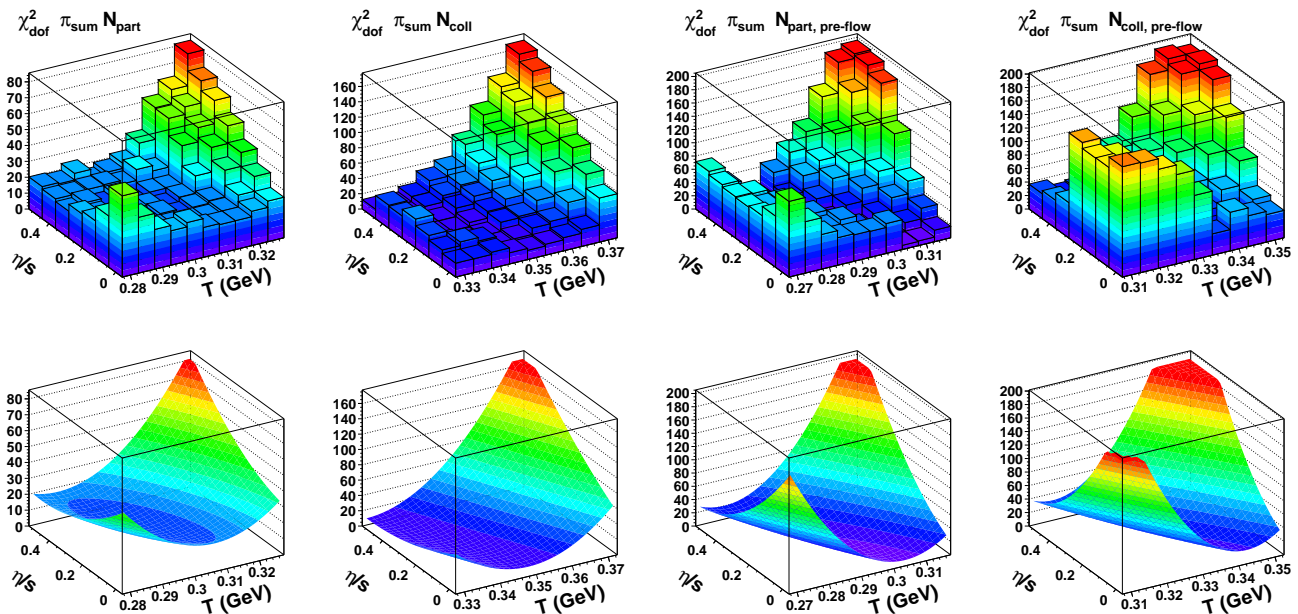


FIG. 16. Equal weight sum of χ_{dof}^2 for pion spectra, elliptic flow, and femtoscopic radii. From left to right the distributions are for N_{part} scaling, N_{coll} scaling, N_{part} scaling with pre-equilibrium flow, and N_{coll} scaling and pre-equilibrium flow. The summed χ_{dof}^2 distributions are on top, and the paraboloid fits are below.

somewhat arbitrary. Although it uses the available statistics to maximal advantage, this is not the same as optimizing the physics extracted. Determining how to select the proper weighting scheme may be the most difficult challenge in the application of CHIMERA-like procedure to constrain the properties of the quark gluon plasma. In order to gain some experience with an alternate weighting scheme, we construct a χ_{dof}^2 sum in which the spectra are weighted by a factor of 10% relative to the other measurements. These χ_{dof}^2 distributions and paraboloid fits are shown in Fig. 17, and the fit parameters are also listed in Table II under the heading Sum₁₀.

In order to study the relationship between the χ_{dof}^2 distributions for each measurement are more easily we plot in Fig. 18 the one- and two-sigma contours obtained from the paraboloid fits. Contours are drawn for the femtoscopic radii (dot-dashed blue), elliptic flow (dotted green), spectra (dashed red), and the 10% spec-weighted sum (solid black). It is instructive to look first at the contours for N_{part} scaling in the upper left. For the three measurements, spectra, elliptic flow, and radii, there is no common overlap at the two-sigma contour level. From Table II, the minimum χ_{dof}^2 values is < 3 for the spectra, and close to 10 for both elliptic flow and radii, but the absence of any overlap in the contours shows that these results are inconsistent with the data. This figure provides a different way of viewing the HBT puzzle. The addition of the pre-equilibrium flow to the N_{part} scaling profile brings raises the temperature of the femtoscopic minimum to a value that is now consistent with the spectra, and the broadening of the v_2 contour creates a region

in which all three contours overlap. The χ_{dof}^2 minimum values are < 5 for all measurements, and the weighted sum χ_{dof}^2 is equal to 6.4, the lowest value for any combined fit.

The N_{coll} scaling contours also display a region of overlap among the three contours, although the χ^2 minima are higher for the radii than for the N_{part} scaling with pre-equilibrium flow. Adding pre-equilibrium flow to the N_{coll} scaling raises the temperature minimum for the pion radii above the spectra, and also produces a much larger χ_{dof}^2 minimum value for the spectra.

V. CONCLUSIONS

We have performed a simultaneous χ^2 evaluation of three measurements: spectra, elliptic flow, and femtoscopic radii from 200 GeV Au+Au collisions for a the 0-20% centrality bin, using using an augmented version of the VH2 viscous 2D+1 hydrodynamic model that incorporates pre-equilibrium flow and initial state eccentricity coupled to the UrQMD hadronic cascade. The evaluation was performed for four sets of initial conditions: N_{part} and N_{coll} initial density profiles with and without the addition of pre-equilibrium flow. The χ^2 evaluation was performed for measurements by the PHENIX and STAR collaborations, and include both statistical and systematic errors. For two of the initial conditions, N_{part} without pre-equilibrium flow, and N_{coll} with pre-equilibrium flow, the constrained regions of T and η/s were mutually exclusive. However, for the N_{part} scaling with pre-

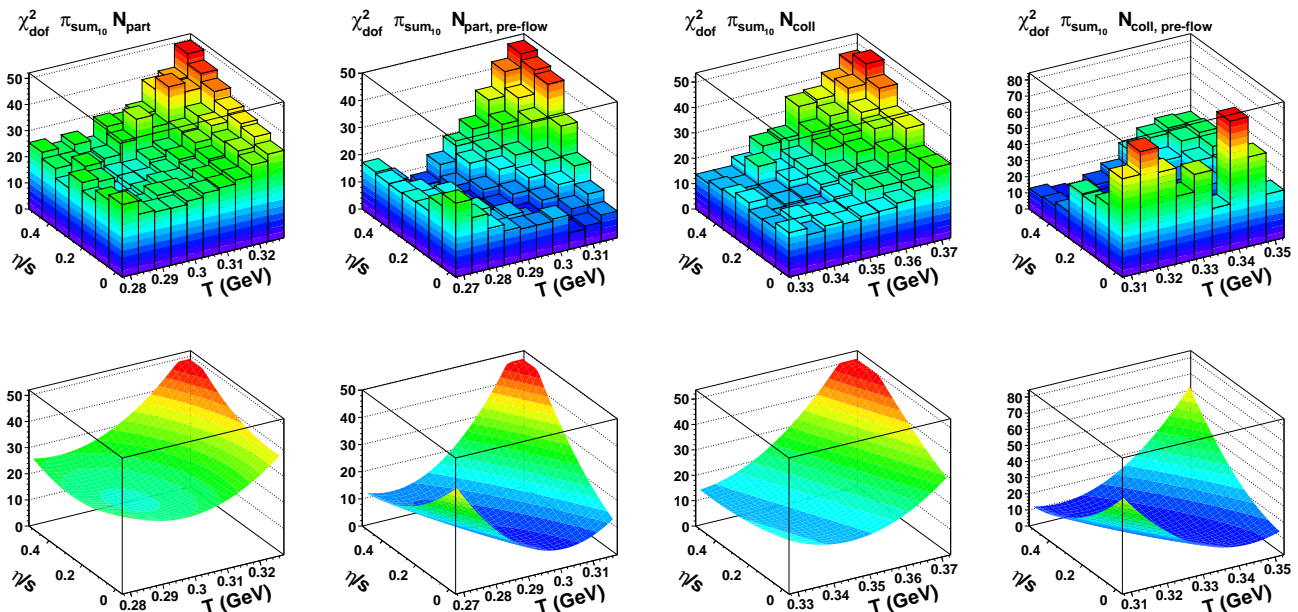


FIG. 17. Sum of χ_{dof}^2 for N_{part} scaling with spectra given 10% weight. From left to right the distributions are for N_{part} scaling, N_{coll} scaling, N_{part} scaling with pre-equilibrium flow, and N_{coll} scaling and pre-equilibrium flow. The weighted sum χ_{dof}^2 distributions are on top, and the paraboloid fits are below.

equilibrium flow and N_{coll} without, the constraints regions overlap at the level of 2σ . This is also the first time that pion radius measurements have been successfully reproduced by a 2D+1 viscous hydrodynamic model coupled to a hadronic cascade.

We regard the main conclusion of this work to be the successful demonstration of an evaluation technique for constraining the multi-parameter space of heavy ion models by comparing to multiple data sets. Working with a relatively small data sample, we were able to achieve a set of constraints for two sets of initial conditions, and to exclude two others. However, the current implementation of CHIMERA should be regarded as incomplete. The centrality matching has room for improvement, the equation of state is not yet specified according to the most recent lattice QCD results, and the full range of initial state profiles has not been explored. There are also additional model parameters, such as τ_{start} and T_{sw} that have not been explored. In addition, the comparisons to experimental data were limited, covering only a single particle species, and a single centrality range. We expect to address these issues in the near future.

Perhaps a more severe limitation on the current implementation of CHIMERA is the inability of VH2 to handle non-smooth initial conditions. Qiu and Heinz have shown that [14] a proper accounting of event by event fluctuations is required to compare to non-central (>60%) collisions is also needed to generate the higher order harmonics that promise to improve our ability to constrain η/s [40, 41]. In order for CHIMERA or a similar framework to ultimately succeed, a more sophisticated 3D+1 hydrodynamic code will need to be used, and its perfor-

mance will need to be evaluated against a wide range of physics observables.

VI. ACKNOWLEDGEMENTS

This work was supported by the U.S. Department of Energy, Grant No. DE-FG02-03ER41259. The authors wish to acknowledge P. Huovinen and D. Molnar for help received when working with the AZHYDRO code, P. Ramatschke for generously sharing his VH2 code, and also S. Bass and the UrQMD working group. We also wish to thank J. Vredevoogd, B. Müller, U. Heinz for insightful discussions. Finally, R. Soltz wishes to thank K. Engle, J. Gearhart, and A. Pavlov for their help identifying errors in the final text and figures.

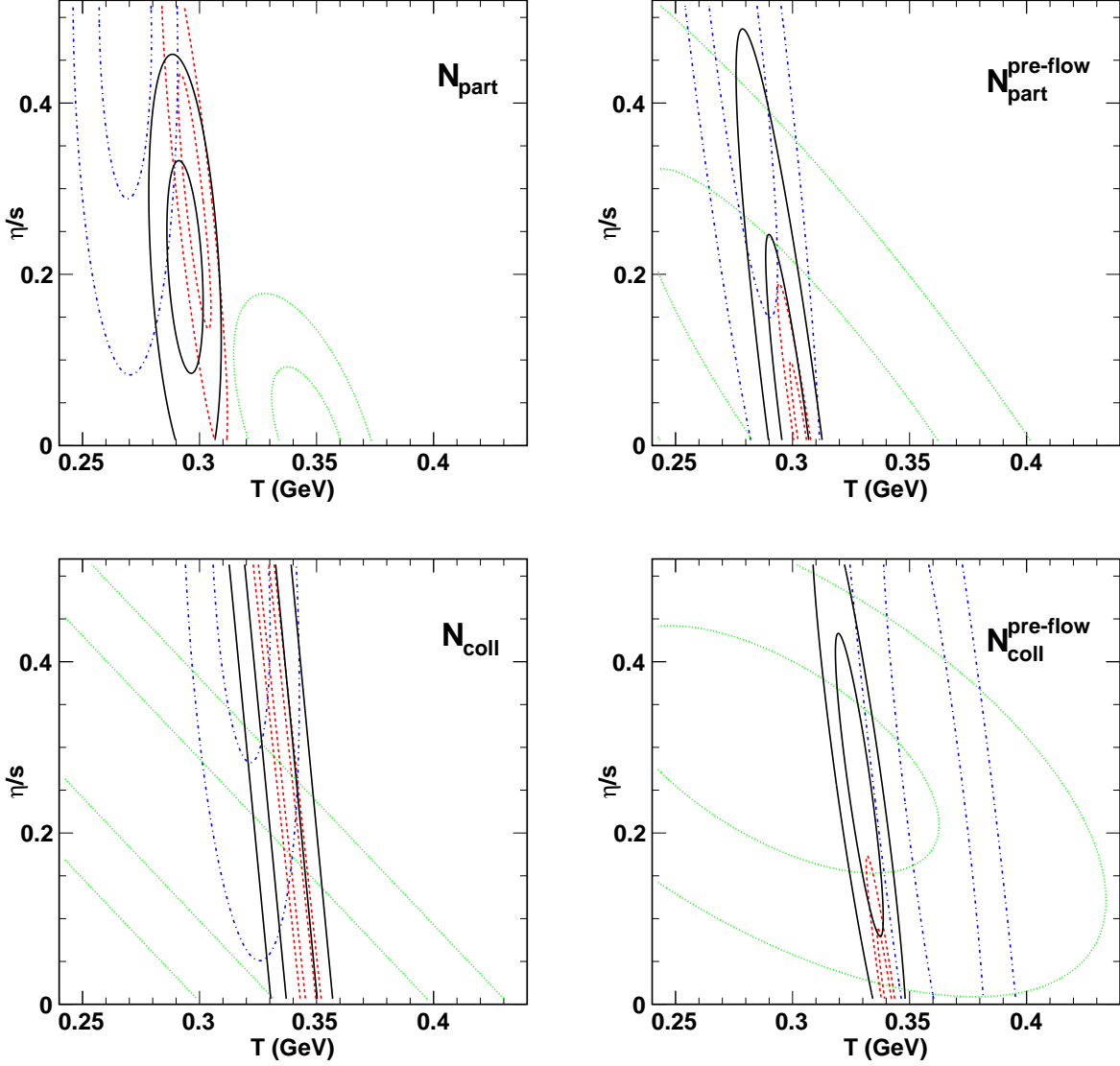


FIG. 18. χ_{dof}^2 contours for pions spectra, elliptic flow, radii, and a weighted sum in which the spectra χ_{dof}^2 are weighted by 10% relative to the other measurements. The four panels show contours for N_{part} scaling (upper left), N_{coll} scaling (lower left), N_{part} with pre-equilibrium flow (upper right), and N_{coll} with pre-equilibrium flow (lower right).

VII. REFERENCES

-
- [1] I. Arsene *et al.* (BRAHMS Collaboratoin), Nuclear Physics A **757**, 1 (2005).
- [2] B. B. Back *et al.* (PHOBOS Collaboration), Nuclear Physics A **757**, 28 (2005).
- [3] J. Adams, M. Aggarwal, Z. Ahammed, J. Amonett, B. Anderson, D. Arkhipkin, G. Averichev, S. Badyal, Y. Bai, and J. Balewski, Phys. Rev. C **72**, 014904 (2005).
- [4] K. Adcox *et al.* (PHENIX Collaboration), Nuclear Physics A **757**, 184 (2005).
- [5] P. Huovinen, P. F. Kolb, U. W. Heinz, P. V. Ruuskanen, and S. A. Voloshin, Phys. Lett. B **503**, 58 (2001).
- [6] P. F. Kolb and U. Heinz, Arxiv preprint nucl-th/0305084 (2003).
- [7] T. Hirano, Phys. Rev. C **65** (2001).
- [8] S. A. Bass, M. Belkacem, M. Bleicher, M. Brandstetter, L. V. Bravina, C. Ernst, L. Gerland, M. Hofmann, S. Hofmann, J. Konopka, G. Mao, L. Neise, S. Soff, C. Spieles, H. Weber, L. A. Winkelmann, H. Stöcker, W. Greiner, C. Hartnack, and J. A. N. Amelin, Prog. Part. Nucl. Phys. **41**, 225 (1998).
- [9] M. Bleicher, E. Zabrodin, C. Spieles, S. A. Bass, C. Ernst, S. Soff, L. Bravina, M. Belkacem, H. Weber, and H. Stöcker, J. Phys. G: Nucl. Part. Phys. **25**, 1859 (1999).
- [10] M. Luzum and P. Romatschke, Phys. Rev. C **78** (2008).
- [11] H. Song, S. Bass, and U. Heinz, Phys. Rev. C **83** (2011).
- [12] T. Kodama, C. E. Aguiar, T. Osada, and Y. Hama, J.Phys.G **G27**, 557 (2001).
- [13] B. Schenke, S. Jeon, and C. Gale, Phys. Rev. C **82** (2010).
- [14] Z. Qiu and U. Heinz, Phys. Rev. C **84** (2011).
- [15] A. Bazavov, T. Bhattacharya, M. Cheng, N. Christ, C. DeTar, S. Ejiri, S. Gottlieb, R. Gupta, U. Heller, K. Huebner, C. Jung, F. Karsch, E. Laermann, L. Levkova, C. Miao, R. Mawhinney, P. Petreczky, C. Schmidt, R. Soltz, W. Soeldner, R. Sugar, D. Toussaint, and P. Vranas, Phys. Rev. D **80** (2009).
- [16] S. Borsányi, G. Endrodi, Z. Fodor, A. Jakovac, S. D. Katz, S. Krieg, C. Ratti, and K. K. Szabó, J. High Energ. Phys. **2010**, 77 (2010).
- [17] H. Song, S. A. Bass, U. Heinz, T. Hirano, and C. Shen, Phys. Rev. Lett. **106**, 192301 (2011).
- [18] B. Alver *et al.* (PHOBOS), Phys. Rev. C **77**, 014906 (2008).
- [19] J. Vredevoogd and S. Pratt, Phys. Rev. C **79** (2009).
- [20] S. Pratt, T. Csörgő, and J. Zimányi, Phys. Rev. C **42**, 2646 (1990).
- [21] D. Brown, A. Enokizono, M. Heffner, R. Soltz, P. Danielewicz, and S. Pratt, Phys. Rev. C **72**, 054902 (2005).
- [22] B. Alver, M. Baker, C. Loizides, and P. Steinberg, arXiv **nucl-ex** (2008).
- [23] M. Laine and Y. Schröder, Phys. Rev. D **73** (2006).
- [24] F. Cooper and G. Frye, Phys. Rev. D **10**, 186 (1974).
- [25] S. Pratt and G. Torrieri, Phys. Rev. C **82** (2010).
- [26] <https://karman.physics.purdue.edu/OSCAR/index.php> (1997).
- [27] C. Amsler and P. D. Grp, Physics Letters B **667**, 1 (2008).
- [28] M. Luzum and P. Romatschke, Phys. Rev. C **79** (2009).
- [29] S. S. Adler *et al.* (PHENIX Collaboration), Phys. Rev. C **69**, 034909 (2004).
- [30] S. Pratt, Phys. Rev. Lett. **102** (2009).
- [31] J.-Y. Ollitrault, A. Poskanzer, and S. Voloshin, Phys. Rev. C **80**, 014904 (2009).
- [32] J. Adams *et al.* (STAR Collaboration), Phys. Rev. Lett. **92**, 112301 (2004).
- [33] K. Adcox *et al.* (PHENIX Collaboration), Phys. Rev. Lett. **88** (2002).
- [34] J. Adams *et al.* (STAR Collaboration), Phys. Rev. C **71**, 044906 (2005).
- [35] S. Adler *et al.* (PHENIX Collaboration), Phys. Rev. Lett. **93** (2004).
- [36] S. Adler *et al.* (PHENIX Collaboration), Phys. Rev. Lett. **91** (2003).
- [37] A. Adare and other (PHENIX Collaboration), Phys. Rev. C **85**, 064914 (2012).
- [38] A. Adare *et al.* (PHENIX Collaboration), Phys. Rev. C **77**, 064907 (2008).
- [39] M. A. Lisa, S. Pratt, R. Soltz, and U. Wiedemann, Annu. Rev. Nucl. Part. Sci. **55**, 357 (2005).
- [40] C. Shen, S. A. Bass, T. Hirano, P. Huovinen, Z. Qiu, H. Song, and U. Heinz, J. Phys. G: Nucl. Part. Phys. **38**, (2011).
- [41] B. Schenke, S. Jeon, and C. Gale, arXiv:1109.6289 **hep-ph** (2011).